6680 *Inorg. Chem.* **2009**, *48*, 6680–6691
DOI: 10.1021/ic900630a

Inorganic Chemistry
Article

Syntheses, Structures and Solid-State Properties of MMX Mixed-Valence Chains, $[Ni^{II/III}_2(RCS_2)_4I]_\infty$ (R = Et, *n*-Pr and *n*-Bu): Evidence of a Spin-Peierls Transition

Minoru Mitsumi,*,† Yuji Yoshida,† Akihisa Kohyama,† Yasutaka Kitagawa,‡ Yoshiki Ozawa,† Mototada Kobayashi,† Koshiro Toriumi,† Makoto Tadokoro,§ Naoshi Ikeda,∥ Mitsutaka Okumura,‡ and Mohamedally Kurmoo⊥

†*Department of Material Science, Graduate School of Material Science, University of Hyogo, 3-2-1 Kouto, Kamigori-cho, Ako-gun, Hyogo 678-1297, Japan,* ‡*Department of Chemistry, Graduate School of Science, Osaka University, 1-1 Machikaneyama, Toyonaka, Osaka 560-0043, Japan,* §*Department of Chemistry, Graduate School of Science, Osaka City University, 3-3-138, Sugimoto, Sumiyoshi-ku, Osaka 558-8585, Japan,* ∥*Japan Synchrotron Radiation Research Institute,1-1 Kouto, Mikazuki-cho, Sayo-gun, Hyogo 679-5198, Japan, and* ⊥*Laboratoire de Chimie de Coordination Organique, CNRS-UMR 7140, Université de Strasbourg, 4 rue Blaise Pascal, F-67000 Strasbourg, France*

Received March 31, 2009

The partial oxidation of $[Ni^{II/II}_2(RCS_2)_4]$ (R = Et (**1**), *n*-Pr (**2**), and *n*-Bu (**3**)) with iodine affords the MMX chain compounds $[Ni^{II/III}_2(RCS_2)_4I]_\infty$ (R = Et (**4**), *n*-Pr (**5**), and *n*-Bu (**6**)), respectively. The crystal structures of **4**−**6** consist of neutral one-dimensional (1-D) chains with a repeating −Ni−Ni−I− unit. The room-temperature (RT) structure of **4** indicates a charge-polarization (CP) state {—$Ni^{(2.5-\delta)+}$—$Ni^{(2.5+\delta)+}$-I^-—$Ni^{(2.5-\delta)+}$—$Ni^{(2.5+\delta)+}$-I^-— ($\delta \ll 0.5$)} close to an averaged valence state judged by the Ni−I distances. In contrast, **5** and **6** exhibit a 3-fold periodicity of a −Ni−Ni−I− unit due to the disorder of the dithiocarboxylato ligands. Compounds **4**−**6** show typical semiconducting behavior and exhibit an intense sharp absorption band centered at 5400 cm^{-1}, which is attributed to a Mott−Hubbard gap due to a relatively large on-site Coulomb repulsion energy *U* of the nickel atoms. The high-temperature magnetic susceptibilities of **4**−**6** can be described by a 1-D Heisenberg antiferromagnetic chain model with $|J|/k_B$ ranging from 898(2) to 939(3) K. Compounds **4** and **5** undergo a spin-Peierls (SP) transition at relatively high T_{sp} = 47 and 36 K, respectively, which are accompanied by superlattice reflections corresponding to a 2-fold −Ni−Ni−I− period below T_{sp}. By determining the superstructure of **4** at 26 K, we conclude that the valence-ordered state changes from the CP in the RT phase to the alternate charge-polarization (ACP) state of —$Ni^{(2.5-\delta)+}$—$Ni^{(2.5+\delta)+}$-I^--$Ni^{(2.5+\delta)+}$—$Ni^{(2.5-\delta)+}$—I^-— in the SP phase. Such a spin-Peierls transition could not be observed for **6**.

1. Introduction

One-dimensional (1-D) halogen-bridged metal complexes, MX chain compounds, have received significant attention for several decades because they display a variety of electronic states originating from the competition between electron−lattice interaction and strong electron−electron correlation.[1] MX chain compounds with M = Pt and Pd are usually in the class II mixed-valence state, -X^-—M^{2+}—X^--M^{4+}-X^-—, and show a shift of the halogen atoms from the midpoint between two metal atoms due to Peierls instability. These class II compounds exhibit characteristic physical properties such as strong intervalence charge-transfer absorption,[2] luminescence with a large Stokes shift,[3] and resonance Raman scattering with long overtone progression[4] originating from the strong electron−lattice interactions. On the other hand, nickel compounds tend to be in a class III averaged-valence state of $-X^--Ni^{3+}-X^--Ni^{3+}-X^--$,

*To whom correspondence should be addressed. Tel.: (+81)791-58-0153. Fax: (+81)791-58-0154. E-mail: mitsumi@sci.u-hyogo.ac.jp.

(1) (a) *Low-dimensional Cooperative Phenomena*; Keller, H. J., Ed.; Plenum Press: New York, 1975; NATO ASI Ser., Ser. B, Vol. 7. (b) Day. P. In *Chemistry and Physics of One-Dimensional Metals*; Keller, H. J., Ed.; Plenum Press: New York, 1977; NATO ASI Ser., Ser. B, Vol. 25, pp 197−223. (c) Soos, Z. G.; Keller, H. J. In *Chemistry and Physics of One-Dimensional Metals*; Keller, H. J., Ed.; Plenum Press: New York, 1977; NATO ASI Ser., Ser. B, Vol. 25, pp 391−412. (d) Keller, H. J. In *Extended Linear Chain Compounds*; Miller, J. S. Ed.; Plenum Press: New York, 1983; Vol. 1, Chapter 8. (e) Clark, R. J. H. *Chem. Soc. Rev.* **1990**, *19*, 107−131. (f) Day, P. *Molecules into Materials: Case Studies in Materials Chemistry−Mixed Valency, Magnetism and Superconductivity*; World Scientific Publishing: Singapore, 2007.

(2) (a) Yamada, S.; Tsuchida, R. *Bull. Chem. Soc. Jpn.* **1956**, *29*, 894–898. (b) Okamoto, H.; Toriumi, K.; Mitani, T.; Yamashita, M. *Phys. Rev. B* **1990**, *42*, 10381–10387.

(3) Tanaka, M.; Kurita, S.; Okada, Y.; Kojima, T.; Yamada, Y. *Chem. Phys.* **1985**, *96*, 343–348.

(4) (a) Clark, R. J. H.; Kurmoo, M. *Inorg. Chem.* **1980**, *19*, 3522–3527. (b) Tanino, H.; Kobayashi, K. *J. Phys. Soc. Jpn.* **1983**, *52*, 1446–1456.

Published on Web 06/10/2009

and the bridging halogen atoms are located at the midpoint between two Ni atoms due to strong electron−electron correlation of the Ni atoms.[5] These Ni compounds are characterized as Mott−Hubbard semiconductors[6] and exhibit very interesting solid-state properties such as gigantic third-order nonlinear optical susceptibility ($\chi^{(3)}$)[7] and an $S = 1/2$ 1-D Heisenberg antiferromagnetic (AF) chain with a strong AF interaction ($|J|/k_B = 3600$ K) between the Ni^{3+} ions.[2b] Using magnetic susceptibility and nuclear quadrupole resonance data, Takaishi et al. recently showed that $\{[NiBr(1R,2R\text{-chxn})_2]Br_2\}_\infty$ (1*R*,2*R*-chxn = 1*R*,2*R*-diaminocyclohexane) undergoes a spin-Peierls (SP) transition in the temperature range of 40−130 K.[8] The Ni compounds have also attracted attention as a 1-D model candidate for high T_c copper oxide superconductors because of the similarity in the electronic band structure to La_2CuO_4, which is the precursor compound to the series $La_{2-x}Sr_xCuO_4$.

The evolution from MX to 1-D halogen-bridged mixed-valence binuclear chain compounds, MMX, has increased this attraction, as MMXs also display a variety of electronic states and a subtle balance of solid-state properties originating from the charge−spin−lattice coupling and the fluctuation of these degrees of freedom. The MMX chain compounds reported so far belong to two families, that is, the pop family of $A_4[Pt_2(pop)_4X]\cdot nH_2O$ (pop = $P_2O_5H_2^{2-}$; A = Li, K, Cs, alkyl ammonium; X = Cl, Br, I)[9] and the dta family (dta = dithioacetato, $MeCS_2^-$) $[M_2(RCS_2)_4I]_\infty$ (M = Pt and R = Me, Et, *n*-Pr, *n*-Bu, *n*-Pen; M = Ni and R = Me).[10−19] These compounds exist in a mixed-valence state composed of M^{2+} (d^8, $S = 0$) and M^{3+} (d^7, $S = 1/2$) with a formal oxidation number of +2.5. Therefore, the MMX chain is a 1-D d−σ electronic system based on a binuclear unit containing a metal−metal bond with a formal bond order of one-half. Important features of MMX compounds are expected to arise from the increase of the internal degrees of freedom resulting from the mixed-valence state of the binuclear unit. This property enables various electronic structures, which are represented by the following four extreme valence-ordered states:

(a) averaged valence (AV) state:
$-M^{2.5+}-M^{2.5+}-X^-\text{-}M^{2.5+}-M^{2.5+}-X^-$

(b) charge-polarization (CP) state:
$—M^{2+}-M^{3+}\text{-}X^-—M^{2+}-M^{3+}\text{-}X^-—$

(c) charge density wave (CDW) state:
$—M^{2+}—M^{2+}—X^-\text{-}M^{3+}\text{-}M^{3+}\text{-}X^-—$

(d) alternate charge-polarization (ACP) state:
$—M^{2+}-M^{3+}\text{-}X^-\text{-}M^{3+}-M^{2+}—X^-—$

The valence state, expressed as a $—M^{2+}-M^{3+}$-, represents an extreme case, which is more accurately represented as $—M^{(2+\delta)+}-M^{(3-\delta)+}$- or $—M^{(2.5-\delta)+}-M^{(2.5+\delta)+}$-. The value of δ depends on the degree of orbital hybridization and lies between the limiting cases of 0 and 0.5. These valence-ordered states are classified on the basis of the periodicity of the 1-D chains as follows. The AV and CP states in which the periodicity of the 1-D chain is −M−M−X− correspond to a metallic state with an effective half-filled conduction band mainly composed of M−M dσ*−X p_z hybridized orbitals or to a Mott−Hubbard semiconducting state. In contrast, the periodicities of the 1-D chains in the CDW and ACP states are doubled. Except for the AV state, the valence-ordered states should undergo lattice distortions due to valence alternation. The magnitude of the on-site Coulomb repulsion U in MMX compounds is relatively small in comparison to MX compounds due to the sharing of one unpaired electron through a metal−metal bond. This facilitates valence delocalization and enhances valence fluctuation in the mixed-valence state. Furthermore, an MMX chain compound should have a strong AF interaction arising from the superexchange interaction between the $S = 1/2$ spins of the M^{3+} ions through the large overlap of the metal d_{z^2} and halogen p_z orbitals, analogous to the Ni MX compounds.[2b]

$[M_2(MeCS_2)_4I]_\infty$ (M = Ni, Pt) were first prepared and characterized by Bellitto et al.[10,11] Soon after, metallic conduction was found for $[Pt_2(MeCS_2)_4I]_\infty$ above 300 K.[12] To reveal the essence of the Pt MMX compound as a 1-D

(5) Toriumi, K.; Wada, Y.; Mitani, T.; Bandow, S.; Yamashita, M.; Fujii, Y. *J. Am. Chem. Soc.* **1989**, *111*, 2341–2342.
(6) Nasu, K. *J. Phys. Soc. Jpn.* **1983**, *52*, 3865–3873.
(7) Kishida, H.; Matsuzaki, H.; Okamoto, H.; Manabe, T.; Yamashita, M.; Taguchi, Y.; Tokura, Y. *Nature* **2000**, *405*, 929–932.
(8) Takaishi, S.; Tobu, Y.; Kitagawa, H.; Goto, A.; Shimizu, T.; Okubo, T.; Mitani, T.; Ikeda, R. *J. Am. Chem. Soc.* **2004**, *126*, 1614–1615.
(9) (a) Che, C.-M.; Herbstein, F. H.; Schaefer, W. P.; Marsh, R. E.; Gray, H. B. *J. Am. Chem. Soc.* **1983**, *105*, 4604–4607. (b) Kurmoo, M.; Clark, R. J. H. *Inorg. Chem.* **1985**, *24*, 4420–4425. (c) Clark, R. J. H.; Kurmoo, M.; Dawes, H. M.; Hursthouse, M. B. *Inorg. Chem.* **1986**, *25*, 409–412. (d) Butler, L. G.; Zietlow, M. H.; Che, C.-M.; Schaefer, W. P.; Sridhar, S.; Grunthaner, P. J.; Swanson, B. I.; Clark, R. J. H.; Gray, H. B. *J. Am. Chem. Soc.* **1988**, *110*, 1155–1162. (e) Stroud, M. A.; Drickamer, H. G.; Zietlow, M. H.; Gray, H. B.; Swanson, B. I. *J. Am. Chem. Soc.* **1989**, *111*, 66–72. (f) Mitani, T.; Wada, Y.; Yamashita, M.; Toriumi, K.; Kobayashi, A.; Kobayashi, H. *Synth. Met.* **1994**, *64*, 291–294. (g) Yamashita, M.; Miya, S.; Kawashima, T.; Manabe, T.; Sonoyama, T.; Kitagawa, H.; Mitani, T.; Okamoto, H.; Ikeda, R. *J. Am. Chem. Soc.* **1999**, *121*, 2321–2322. (h) Matsuzaki, H.; Matsuoka, T.; Kishida, H.; Takizawa, K.; Miyasaka, H.; Sugiura, K.; Yamashita, M.; Okamoto, H. *Phys. Rev. Lett.* **2003**, *90*, 046401 (4 pages). (i) Mastuzaki, H.; Kishida, H.; Okamoto, H.; Takizawa, K.; Matsunaga, S.; Takaishi, S.; Miyasaka, H.; Sugiura, K.; Yamashita, M. *Angew. Chem., Int. Ed.* **2005**, *44*, 3240–3243. (j) Yamashita, M.; Takaishi, S.; Kobayashi, A.; Kitagawa, H.; Matsuzaki, H.; Okamoto, H. *Coord. Chem. Rev.* **2006**, *250*, 2335–2346. (k) Iguchi, H.; Takaishi, S.; Kajiwara, T.; Miyasaka, H.; Yamashita, M.; Matsuzaki, H.; Okamoto, H. *J. Am. Chem. Soc.* **2008**, *130*, 17668–17669.
(10) (a) Bellitto, C.; Flamini, A.; Gastaldi, L.; Scaramuzza, L. *Inorg. Chem.* **1983**, *22*, 444–449. (b) Bellitto, C.; Dessy, G.; Fares, V. *Inorg. Chem.* **1985**, *24*, 2815–2820. (c) Clark, R. J. H.; Walton, J. R. *Inorg. Chim. Acta* **1987**, *129*, 163–171.
(11) (a) Yamashita, M.; Wada, Y.; Toriumi, K.; Mitani, T. *Mol. Cryst. Liq. Cryst.* **1992**, *216*, 207–212. (b) Shirotani, I.; Kawamura, A.; Yamashita, M.; Toriumi, K.; Kawamura, H.; Yagi, T. *Synth. Met.* **1994**, *64*, 265–270.
(12) Kitagawa, H.; Onodera, N.; Sonoyama, T.; Yamamoto, M.; Fukawa, T.; Mitani, T.; Seto, M.; Maeda, Y. *J. Am. Chem. Soc.* **1999**, *121*, 10068–10080.
(13) Mitsumi, M.; Murase, T.; Kishida, H.; Yoshinari, T.; Ozawa, Y.; Toriumi, K.; Sonoyama, T.; Kitagawa, H.; Mitani, T. *J. Am. Chem. Soc.* **2001**, *123*, 11179–11192.
(14) Mitsumi, M.; Kitamura, K.; Morinaga, A.; Ozawa, Y.; Kobayashi, M.; Toriumi, K.; Iso, Y.; Kitagawa, H.; Mitani, T. *Angew. Chem., Int. Ed.* **2002**, *41*, 2767–2771.
(15) Mitsumi, M.; Umebayashi, S.; Ozawa, Y.; Toriumi, K.; Kitagawa, H.; Mitani, T. *Chem. Lett.* **2002**, *31*, 258–259.
(16) (a) Tanaka, H.; Kuroda, S.; Yamashita, T.; Mitsumi, M.; Toriumi, K. *J. Phys. Soc. Jpn.* **2003**, *72*, 2169–2172. (b) Mitsumi, M.; Yamashita, T.; Toriumi, K. Unpublished.
(17) (a) Wakabayashi, Y.; Kobayashi, A.; Sawa, H.; Ohsumi, H.; Ikeda, N.; Kitagawa, H. *J. Am. Chem. Soc.* **2006**, *128*, 6676–6682. (b) Otsubo, K.; Kobayashi, A.; Kitagawa, H.; Hedo, M.; Uwatoko, Y.; Sagayama, H.; Wakabayashi, Y.; Sawa, H. *J. Am. Chem. Soc.* **2006**, *128*, 8140–8141.
(18) (a) Borshch, S. A.; Prassides, K.; Robert, V.; Solonenko, A. O. *J. Chem. Phys.* **1998**, *109*, 4562–4568. (b) Robert, V.; Petit, S.; Borshch, S. A. *Inorg. Chem.* **1999**, *38*, 1573–1578. (c) Calzolari, A.; Alexandre, S. S.; Zamora, F.; Felice, R. D. *J. Am. Chem. Soc.* **2008**, *130*, 5552–5562.
(19) (a) Nakano, S.; Kitagawa, Y.; Kawakami, T.; Yamaguchi, K. *Polyhedron* **2003**, *22*, 2027–2038. (b) Kitagawa, Y.; Shoji, M.; Koizumi, K.; Kawakami, T.; Okumura, M.; Yamaguchi, K. *Polyhedron* **2007**, *26*, 2154–2160.

electronic system, we have studied the series of MMX chain compounds, $[Pt_2(RCS_2)_4I]_\infty$ (R = Et,[13,14] *n*-Pr,[15] *n*-Bu,[14] *n*-Pen[16]), and have investigated the correlation between their crystal structures and solid-state properties. It was found that $[Pt_2(RCS_2)_4I]_\infty$ (R = Et, *n*-Bu, *n*-Pen) are in the AV state at room temperature (RT) and exhibit metallic behavior above 205−324 K.[13,14,16] From the crystal structure analyses, the valence-ordered states of $[Pt_2(RCS_2)_4I]_\infty$ (R = Et, *n*-Bu) at low temperatures (LT) are considered to be the ACP state.[14] Furthermore, we have established the origin of the electronic localization for $[Pt_2(n\text{-}BuCS_2)_4I]_\infty$ to be a regular Peierls transition since this transition to the ACP state is accompanied by a rapid decrease in the conductivity and magnetic susceptibility. In contrast, $[Ni_2(MeCS_2)_4I]_\infty$ has an AV state at RT but exhibits a sharp peak near 0.6 eV in the reflectance spectrum for light polarized parallel to the 1-D chain, which is attributed to a Mott−Hubbard gap due to a relatively large on-site Coulomb repulsion energy U of the nickel atoms.[11a] Accordingly, this compound is regarded as a Mott−Hubbard semiconductor. However, the spin-Peierls transition expected for an $S = 1/2$ 1-D Heisenberg AF chain at LT has not been observed, and therefore the valence-ordered state remains unclear. To clarify the valence-ordered state at LT and to realize the spin-Peierls state in the Ni MMX system, it is important to control interchain interactions by the chemical modification of the alkyl group of the dithiocarboxylato ligand.

We therefore decided to synthesize the series of MMX chain compounds $[Ni_2(RCS_2)_4I]_\infty$ (R = Et (**4**), *n*-Pr (**5**), and *n*-Bu (**6**)) from their corresponding precursors $[Ni_2(RCS_2)_4]_\infty$ (R = Et (**1**), *n*-Pr (**2**), and *n*-Bu (**3**)) by an oxidative-addition reaction with molecular iodine. We report herein the results of the syntheses, crystal structures, and solid-state properties of these Ni MMX chain compounds **4**−**6** and demonstrate that **4** and **5** undergo a spin-Peierls transition with a relatively high transition temperature of T_{sp} = 47 and 36 K, respectively. These are the first examples of 1-D MMX compounds to display a spin-Peierls transition.

2. Experimental Section

Syntheses. Unless otherwise stated, all manipulations were performed at room temperature under an argon atmosphere with standard vacuum line and Schlenk techniques. All solvents were dried using appropriate drying agents and freshly distilled under argon before use.[20] Dithiopropanoic acid, $EtCS_2H$; dithiobutanoic acid, *n*-$PrCS_2H$; and dithiopentanoic acid, *n*-$BuCS_2H$ were prepared according to published procedures.[21] Elemental analyses were performed at the Center for Organic Elemental Microanalysis of the Graduate School of Pharmaceutical Sciences, Kyoto University.

$[Ni_2(EtCS_2)_4]$ (1). For the synthesis of this compound, we adopted a slight modification of the method described in ref 30. A solution of dithiopropanoic acid (2.970 g, 27.96 mmol) in 38 mL of ether was added dropwise with stirring to a solution of $NiCl_2\cdot 6H_2O$ (6.540 g, 27.51 mmol) in 27 mL of ethanol, to produce a dark red mixture. The reaction mixture was stirred for an additional 30 min at room temperature. It was then cooled to 0 °C and allowed to stand for 1 h. On cooling, reddish black microcrystals separated from the solution. These were collected and washed with ether. The crude product was recrystallized from benzene−*n*-hexane to afford 2.340 g (62% yield based on dithiopropanoic acid) of $[Ni_2(EtCS_2)_4]$ as lustrous reddish black needles. Anal. calcd for $C_{12}H_{20}Ni_2S_8$: C, 26.78; H, 3.75. Found: C, 26.74; H, 3.69%.

$[Ni_2(n\text{-}PrCS_2)_4]$ (2). Compound **2** was obtained by a similar method to that of **1** using dithiobutanoic acid (5.051 g, 42.01 mmol) in 42 mL of ether and $NiCl_2\cdot 6H_2O$ (9.482 g, 39.89 mmol) in 29 mL of ethanol. The crude product was recrystallized from benzene−*n*-hexane to afford 4.049 g (65% yield based on dithiobutanoic acid) of $[Ni_2(n\text{-}PrCS_2)_4]$ as lustrous reddish black needles. Anal. calcd for $C_{16}H_{28}Ni_2S_8$: C, 32.34; H, 4.75. Found: C, 32.56; H, 4.71%.

$[Ni_2(n\text{-}BuCS_2)_4]$ (3). Compound **3** was obtained by a similar method to that of **1** using dithiopentanoic acid (1.650 g, 12.29 mmol) in 20 mL of ether and $NiCl_2\cdot 6H_2O$ (3.010 g, 12.66 mmol) in 15 mL of ethanol. The crude product was recrystallized from *n*-hexane to afford 1.021 g (51% yield based on dithiopentanoic acid) of $[Ni_2(n\text{-}BuCS_2)_4]$ as lustrous reddish black needles. Anal. calcd for $C_{20}H_{36}Ni_2S_8$: C, 36.93; H, 5.58. Found: C, 36.77; H, 5.38%.

$[Ni_2(EtCS_2)_4I]_\infty$ (4). $[Ni_2(EtCS_2)_4]$ (608 mg, 1.13 mmol) was dissolved in 110 mL of a mixture of *n*-hexane−CS_2 (1:1), and then iodine vapor (110 mg, 0.433 mmol) was allowed to diffuse slowly into the solution at 5−6 °C. After standing for 1−2 weeks, the deposited black needle crystals of **4** were collected by suction filtration and dried under vacuum conditions. Yield: 54 mg (7%). Anal. calcd for $C_{12}H_{20}INi_2S_8$: C, 21.67; H, 3.03. Found: C, 21.65; H, 2.99%.

$[Ni_2(n\text{-}PrCS_2)_4I]_\infty$ (5). Black needle crystals of **5** were obtained by a similar method to that of **4** using **2** (1.002 g, 1.686 mmol) in 105 mL of *n*-hexane−benzene (1:1) and iodine (192 mg, 0.756 mmol). Yield: 40 mg (3%). Anal. calcd for $C_{16}H_{28}INi_2S_8$: C, 26.65; H, 3.91. Found: C, 26.66; H, 3.89%.

$[Ni_2(n\text{-}BuCS_2)_4I]_\infty$ (6). Black needle crystals of **6** were obtained by a similar method to that of **4** using **3** (495 mg, 0.761 mmol) in 30 mL of *n*-hexane−CS_2 (8:1) and iodine (50 mg, 0.20 mmol). Yield: 23 mg (4%). Anal. calcd for $C_{20}H_{36}INi_2S_8$: C, 30.90; H, 4.67. Found: C, 30.91; H, 4.56%.

UV−Visible−Near-IR and Mid-IR Spectroscopy. UV−visible−near-IR spectra of the compounds were recorded on a Hitachi U-3500 spectrophotometer equipped with a 60 mmϕ integrating-sphere apparatus. Mid-IR spectra for **1**−**3** were recorded on a Horiba FT-200 spectrophotometer, and those for **4**−**6** were measured on a JASCO FT/IR-4000 spectrophotometer. The measurements were carried out using KBr pressed disks for **1**−**3** and both KBr and KI disks for **4**−**6**.

X-Ray Crystal Structure Analyses. A summary of the crystallographic data and intensity data collection for all structures is given in Table 1. Crystallographic information files (CIF) for all data sets are listed in the Supporting Information.

$[Ni_2(EtCS_2)_4I]_\infty$ (4) at 292 K and $[Ni_2(n\text{-}BuCS_2)_4I]_\infty$ (6) at 290 K. Crystals were mounted on glass fibers using Apiezon grease. X-ray diffraction measurements were made using Mo Kα radiation of λ = 0.71070 Å on a Rigaku AFC7 Mercury CCD diffractometer equipped with a Rigaku variable-temperature apparatus on the basis of a cold nitrogen gas stream method at the Graduate School of Science, Osaka City University. Cell refinements, indexing, peak integrations, and scaling of the diffraction data were carried out using the CrystalClear software. Lorentz, polarization, and a numerical absorption correction were applied to the intensity data.

$[Ni_2(n\text{-}PrCS_2)_4I]_\infty$ (5) at 240 and 140 K. All measurements were carried out on a Rigaku RAXIS-RAPID imaging plate

(20) Perrin, D. D.; Armarego, W. L. F. *Purification of Laboratory Chemicals*; Pergamon Press: New York, 1988.
(21) Hartke, K.; Rettberg, N.; Dutta, D.; Gerber, H.-D. *Liebigs Ann. Chem.* **1993**, 1081–1089.
(22) (a) DENZO and SCALEPACK: Otwinowski, Z.; Minor, W. *Methods Enzymol.* **1997**, *276*, 307−326. (b) PLATON: Spek, A. L. *J. Appl. Crystallogr.* **2003**, *36*, 7−13.
(23) (a) SIR97: Altomare, A.; Burla, M. C.; Camalli, M.; Cascarano, G. L.; Giacovazzo, C.; Guagliardi, A.; Moliterni, A. G. G.; Polidori, G.; Spagna, R. *J. Appl. Crystallogr.* **1999**, *32*, 115−119. (b) Sheldrick, G. M. *SHELXL-97*; University of Göttingen: Göttingen, Germany, 1997.

Table 1. Crystal Data and Details of Structure Refinement for **4**−**6**

compound	**4**	**4**	**5**	**5**	**5**	**6**
formula	$C_{12}H_{20}INi_2S_8$	$C_{12}H_{20}INi_2S_8$	$C_{16}H_{28}INi_2S_8$	$C_{16}H_{28}INi_2S_8$	$C_{16}H_{28}INi_2S_8$	$C_{20}H_{36}INi_2S_8$
fw	665.11	665.11	721.22	721.22	721.22	777.33
T, K	292	26	240	140	31	290
cryst size, mm^3	0.13×0.11×0.11	0.307×0.091×0.023	0.235×0.09×0.08	0.235×0.09×0.08	0.195×0.136×0.114	0.320×0.15×0.12
wavelength, Å	0.71070	0.5646(8)	0.71075	0.71075	0.5640(4)	0.71070
cryst syst	monoclinic	triclinic	monoclinic	monoclinic	monoclinic	tetragonal
space group	$C2/c$	$P\bar{1}$	$C2/m$	$C2$	$C2$	$P4/mnc$
a, Å	17.274(3)	9.538(1)	17.7659(5)	37.2403(8)	37.072(1)	13.4900(17)
b, Å	8.3751(14)	15.125(1)	25.1099(8)	8.3633(2)	8.355(1)	13.4900(17)
c, Å	16.745(3)	15.725(1)	13.0451(5)	18.0518(5)	17.987(1)	25.000(3)
α, deg	90	99.109(3)	90	90	90	90
β, deg	114.459(3)	102.214(3)	136.4426(8)	112.8310(7)	113.2810(10)	90
γ, deg	90	98.632(4)	90	90	90	90
V, Å^3	2205.1(7)	2149.2(3)	4010.0(2)	5181.8(2)	5117.6(7)	4549.4(9)
Z	4	4	6	8	8	6
D_c, g cm^{-3}	2.003	2.055	1.792	1.849	1.872	1.702
μ, mm^{-1}	3.859	1.960	3.191	3.293	1.652	2.820
F(000)	1 316	1 316	2 166	2 888	2 888	2 358
θ_{min}, θ_{max}, deg	3.29, 27.48	1.10, 28.14	3.12, 30.02	3.02, 29.99	1.61, 28.03	3.13, 27.48
no. of total reflns	9977	21762	22908	30788	21327	7561
no. of unique reflns	2455	14121	5976	12840	15557	2640
R_{int}	0.0281	0.0193	0.0422	0.0293	0.0195	0.0490
no. of observed [$I > 2\sigma(I)$]	2264	7835	4546	11732	15434	1766
R1, wR2 [$I > 2\sigma(I)$]	0.0276, 0.0549	0.0482, 0.1198	0.0530, 0.1074	0.0309, 0.0761	0.0361, 0.1035	0.0593, 0.1499
R1, wR2 (all data)	0.0337, 0.0566	0.0651, 0.1301	0.0757, 0.1150	0.0349, 0.0785	0.0363, 0.1036	0.0960, 0.1627
GOF	1.180	1.158	1.199	1.062	1.141	1.169
max, min $\Delta\rho$, e Å^{-3}	0.427 /−0.319	0.919/−1.224	0.634/−2.104	1.558/−0.637	1.487/−1.683	1.322/−0.554

diffractometer with graphite-monochromated Mo Kα radiation (λ = 0.71075 Å), equipped with a Rigaku variable-temperature apparatus. Cell refinements, indexing, peak integrations, and scaling of the diffraction data sets were carried out using the program RAPID AUTO. Lorentz, polarization, and a numerical absorption correction were applied to the intensity data.

$[Ni_2(EtCS_2)_4I]_\infty$ (4) at 26 K and $[Ni_2(n\text{-}PrCS_2)_4I]_\infty$ (5) at 31 K. Single crystals were mounted on carbon fibers. These crystals were attached to a closed-cycle helium cryostat. Diffraction data were collected under vacuum conditions (1.5×10^{-3} Pa) using synchrotron radiation (21.96 keV, λ = 0.5646(8) Å, for **4** and 21.98 keV, λ = 0.5640(4) Å, for **5**) and a MAC Science low-temperature vacuum X-ray camera equipped with an imaging plate area detector at the BL02B1 beamline of SPring-8. The reflections of each frame were indexed and integrated using DENZO and subsequently scaled using SCALEPACK.[22a] An empirical correction for absorption anisotropy was applied to all intensity data using PLATON-MULABS.[22b]

Structure Solution and Refinements. The structures were solved by direct methods (SIR97) and expanded using Fourier techniques.[23a] All refinements were made on F^2 with full-matrix least-squares methods using the SHELXL97 program.[23b] All non-hydrogen atoms in **6** were refined anisotropically, except for the C7 atom, which was refined isotropically. Hydrogen atoms were placed at the positions calculated geometrically.

X-Ray Photoelectron Spectroscopy. X-ray photoelectron spectroscopy (XPS) data were obtained using a VG ESCALAB 220i-XL spectrometer equipped with non-monochromatized Mg Kα (1253.6 eV). The X-ray source was operated at 15 kV and 10 mA. Measurements were carried out with the samples held in the 10^{-6} Pa pressure range. Samples were powdered and spread on conductive adhesive tape attached to sample holders. The absence of X-ray beam effects was checked by the X-ray power dependence of the XPS spectra. The carbon 1s binding energy (284.6 eV) was used to calibrate the binding energy scale.[24] Curve fitting analyses to determine binding energies and relative intensities were performed with an iterative least-squares computer program, XPSPEAK41, using a combination of Gaussian and Lorenztian line shapes to best fit the experimentally observed envelope.[25]

Electrical Transport Measurements. Direct current electrical conductivity measurements of **4**−**6** along the 1-D chain direction were made on several single crystals in temperature ranges of 250−300 K (**4** and **5**) and 165−287 K (**6**) using a four-probe technique. Electrical contacts on the samples were made with gold paint to 20 $\mu m\phi$ gold wires. The sample was placed in a liquid-nitrogen cryostat with helium as the exchange gas, in which the temperature was monitored through a calibrated Au(Fe)−chromel thermocouple located in close proximity to the samples.

Magnetic Susceptibility. Measurements were made using a Quantum Design MPMS-5 SQUID magnetometer in the temperature range of 2−328 K in a field of 1 T. Corrections for core diamagnetism for **4**−**6** were made using the sum of the diamagnetism of **1**−**3** and half the Pascal constant of iodine.[26]

DFT Calculation. In order to carry out DFT calculations for $[Ni_2(MeCS_2)_4I]_\infty$, we constructed a model structure which consisted of two binuclear $(MM)_2$ units, as illustrated in Figure S1 (Supporting Information). Atomic coordinates of the model structure were taken from the X-ray crystallographic data of Bellitto et al.[10b] All calculations were performed using the unrestricted B3LYP (UB3LYP)[27] method with the basis sets of Tatewaki−Huzinaga MIDI plus the p-type function (533(21)/53(21)/(41)) for Ni atoms,[28] MIDI plus the d-type function (3333(21)/333(21)/331) for iodide atoms,[28] and 4-31G for $MeCS_2$ ligands.[29]

(24) *Handbook of X-ray Photoelectron Spectroscopy*; Wagner, C. D., Riggs, W. M., Davis, L. E., Moulder, J. F., Mullenberg, G. E., Eds.; Perkin-Elmer Corporation: Waltham, MA.

(25) Kwok, R. W. M. *XPSPEAK41*, XPS Peak Fitting Program for WIN95/98 XPSPEAK, version 4.1; Hong Kong, 2000.

(26) Kahn, O. *Molecular Magnetism*; VCH Publishers: New York, 1993.

(27) Becke, A. D. *J. Chem. Phys.* **1993**, *98*, 5648–5652.

(28) *Gaussian Basis Sets for Molecular Calculations*; Huzinaga, S., Ed.; Elsevier: New York, 1984, Physical Sciences Data 16.

(29) The calculations were preformed using Gaussian 98 software: Frisch, M. J. *Gaussian 98*, revision A.11.3; Gaussian, Inc.: Pittsburg, PA, 2002.

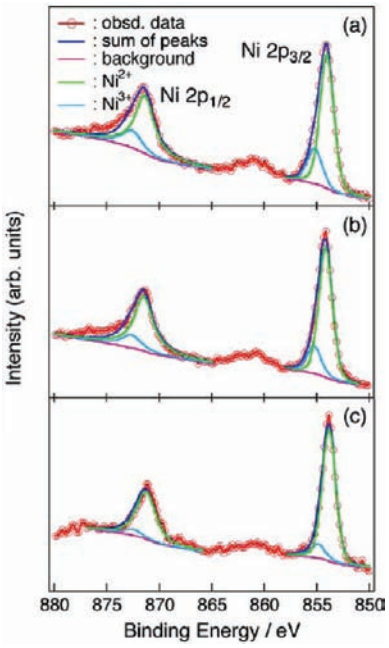

Figure 1. The Ni $2p_{3/2}$ and $2p_{1/2}$ core level spectra for (a) $[Ni_2(EtCS_2)_4I]_\infty$ (**4**), (b) $[Ni_2(n\text{-}PrCS_2)_4I]$ (**5**), and (c) $[Ni_2(n\text{-}BuCS_2)_4I]$ (**6**). The solid lines are the deconvoluted and sum of the components.

Table 2. Binding Energy (eV) and Width of the Peaks[a,b] from the XPS Data for **1**−**6**

compound	Ni^{2+} $2p_{3/2}$	Ni^{3+} $2p_{3/2}$	Ni^{2+} $2p_{1/2}$	Ni^{3+} $2p_{1/2}$
1	854.09 (1.53)		871.29 (2.08)	
2	854.05 (1.53)		871.18 (2.03)	
3	854.22 (1.56)		871.38 (1.98)	
4	854.04 (1.53)	855.21 (1.68)	871.37 (2.18)	872.61 (2.23)
5	854.16 (1.55)	855.26 (1.59)	871.47 (2.15)	872.65 (2.21)
6	853.86 (1.53)	854.90 (1.53)	871.26 (2.20)	872.50 (2.20)

[a] Full width at half-maximum values (fwhm) for peaks are given in parentheses. [b] These values were corrected against the C 1s peak using a value of 284.6 eV.

3. Results and Discussion

X-Ray Photoelectron Spectra. To examine the valence states of the nickel atoms, X-ray photoelectron spectra (XPS) of the $Ni^{2+}-Ni^{3+}$ compounds **4**−**6** were measured at room temperature together with those of the corresponding $Ni^{2+}-Ni^{2+}$ compounds **1**−**3**. The Ni $2p_{3/2}$ and $2p_{1/2}$ core level spectra for the mixed-valent compounds are shown in Figure 1 and those of the divalent compounds in Figure S2 (Supporting Information). Binding energies of the Ni $2p_{3/2}$ and $2p_{1/2}$ core level are summarized in Table 2. The Ni $2p_{3/2}$ and $2p_{1/2}$ peaks of **4**−**6** were broad compared to those of the corresponding complexes **1**−**3** and could be resolved into Ni^{2+} $2p_{3/2,1/2}$ and Ni^{3+} $2p_{3/2,1/2}$ doublets using curve deconvolution employing a Gaussian−Lorentzian line shape fit. The results revealed that **4**−**6** exist in the mixed-valence state composed of Ni^{2+} and Ni^{3+} on the time scale of XPS spectroscopy (ca. 10^{-17} s). Although the peak area ratio of Ni^{2+} $2p_{3/2,1/2}$ and Ni^{3+} $2p_{3/2,1/2}$ doublets of **4**−**6** should be equal because of the $Ni^{2+}-Ni^{3+}$ mixed-valence state, the intensity of the Ni^{3+} $2p_{3/2,1/2}$ doublet is very weak compared to that of Ni^{2+}. This would be due to the reduction of Ni^{3+} to Ni^{2+} by X-ray irradiation, similar to the observation made for $[Pt_2(EtCS_2)_4I]_\infty$.[13]

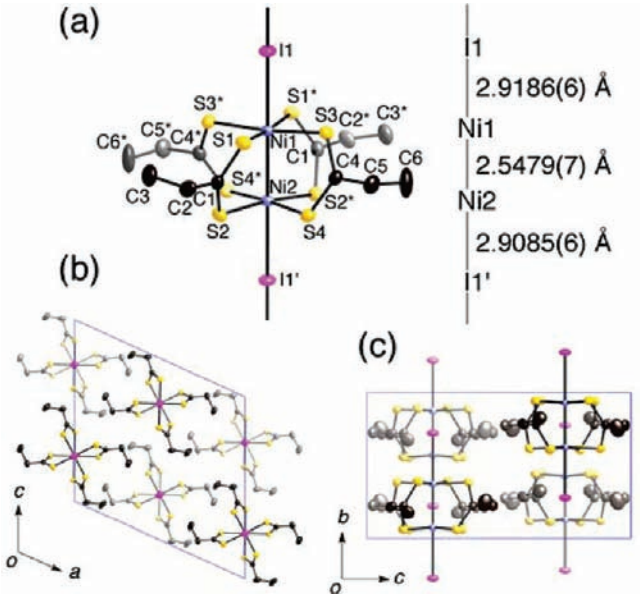

Figure 2. (a) 1-D chain structure of $[Ni_2(EtCS_2)_4I]_\infty$ (**4**) at 292 K with an atomic numbering scheme and relevant interatomic distances (thermal ellipsoid set at the 50% probability level). Packing diagrams projected down the (b) *b* and (c) *a* axes.

Crystal Structure of $[Ni_2(EtCS_2)_4I]_\infty$ (4). An ORTEP diagram of the structures of **4** at 292 K is shown in Figure 2. Compound **4** crystallizes in the monoclinic space group *C*2/*c*, as that of the RT phase of $[Pt_2(EtCS_2)_4I]_\infty$.[13] The structure consists of neutral 1-D chains with a repeating −Ni−Ni−I− unit lying along the crystallographic 2-fold axis parallel to the *b* axis. Two nickel atoms are bridged by four dithiopropanato ligands, and the Ni−Ni distance is 2.5479(7) Å, which is 0.22 Å shorter than the distance between the mean planes defined by the four sulfur atoms (2.77(3) Å). This Ni−Ni distance is marginally shorter than that of the dinuclear $Ni^{2+}-Ni^{2+}$ complex, $[Ni_2(MeCS_2)_4]$ (2.564(1) Å), but longer than $[Ni_2(EtCS_2)_4]$ (2.5267(10) Å).[30] The two NiS_4 square planes are twisted by 28.2(9)° from the eclipsed structure. The twist angle slightly decreases with a lengthening of the Ni−Ni distance compared with that of $[Ni_2(EtCS_2)_4]$ (29.68(3)°).[30] In the case of diplatinum complexes, it is known that the Pt−Pt distance tends to shorten with an increase in the formal oxidation state of the platinum atoms due to the Pt−Pt bond formation by the removal of an electron from the filled dσ* orbital.[13,31] In contrast, the Ni−Ni distance appears to be strongly influenced by the interaction with the surrounding atoms rather than by the formal oxidation state of the nickel atoms, that is, Ni−I interaction in **4**, intermolecular Ni···S interaction in $[Ni_2(MeCS_2)_4]$,[10b] and intermolecular Ni···Ni interaction in $[Ni_2(EtCS_2)_4]$,[30] in addition to the packing effect, including the twist angle of the two NiS_4 planes. Therefore, the tendency for the M−M distance to shorten with

(30) Kobayashi, A.; Kojima, T.; Ikeda, R.; Kitagawa, H. *Inorg. Chem.* **2006**, *45*, 322–327.
(31) (a) Mitsumi, M.; Yoshinari, T.; Ozawa, Y.; Toriumi, K. *Mol. Cryst. Liq. Cryst.* **2000**, *342*, 127–132. (b) Mitsumi, M.; Ueda, H.; Furukawa, K.; Ozawa, Y.; Toriumi, K.; Kurmoo, M. *J. Am. Chem. Soc.* **2008**, *130*, 14102–14104. (c) Bellitto, C.; Bonamico, M.; Dessy, G.; Fares, V.; Flamini, A. J. *Chem. Soc., Dalton Trans.* **1986**, 595–601.

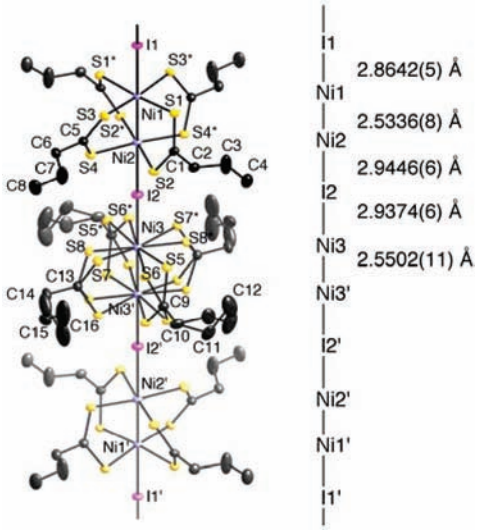

Figure 3. 1-D chain structure of $[Ni_2(n\text{-}PrCS_2)_4I]_\infty$ (**5**) in the RT phase at 240 K with an atomic numbering scheme and relevant interatomic distances (thermal ellipsoid set at the 30% probability level).

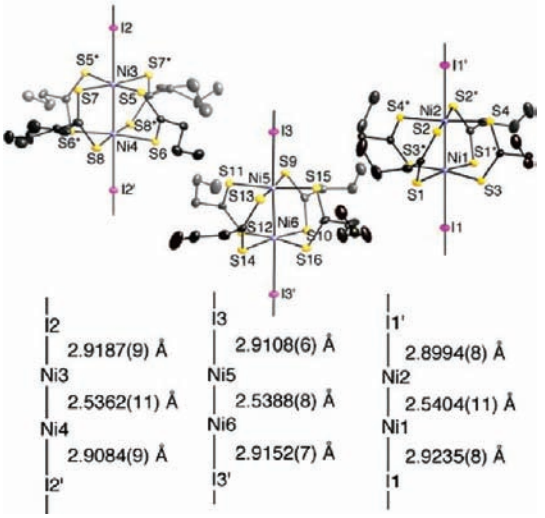

Figure 4. 1-D chain structures of $[Ni_2(n\text{-}PrCS_2)_4I]_\infty$ (**5**) in the LT phase at 140 K with an atomic numbering scheme and relevant interatomic distances (thermal ellipsoid set at the 50% probability level).

an increase in the formal oxidation state is not a criterion for the dinickel complex. The two Ni−I distances are Ni1−I1 = 2.9186(6) and Ni2−I1′ = 2.9085(6) Å, and the bridging iodine atom slightly deviates from the midpoint of the binuclear units. Generally, the $Ni^{2+}-I^-$ distance is longer than that of $Ni^{3+}-I^-$ since a pair of electrons occupies the d_{z^2} orbital of Ni^{2+}, and therefore the difference between the Ni−I distances indicates a charge disproportionation of the nickel atoms. Taking into account the distinct difference of Ni−I distances, the valence-ordered state of **4** at RT should be assigned to a CP state of $—Ni^{(2.5-\delta)+}-Ni^{(2.5+\delta)+}\text{-}I^-—Ni^{(2.5-\delta)+}-Ni^{(2.5+\delta)+}\text{-}I^-—$ ($\delta \ll 0.5$) close to an AV state. In the case of $[Ni_2(MeCS_2)_4I]_\infty$, the shorter interchain S···S distances are 3.619(8) and 3.810(5) Å, which are relatively close to the van der Waals contact distance between sulfur atoms (3.60 Å).[10b,32] However, the shorter interchain S···S distances in **4** are S(4)···S(4) ($-x$, $1-y$, $1-z$) = 4.359(1) Å and S(3)···S(3) ($-x$, $-y$, $1-z$) = 4.973(1) Å, indicating no interchain S···S contacts. Therefore, the one-dimensionality of **4** is enhanced by the introduction of the ethyl group into the dithiocarboxylato ligand instead of the methyl group.

Crystal Structure of $[Ni_2(n\text{-}PrCS_2)_4I]_\infty$ (5). The differential scanning calorimetry measurements of **5** indicate that a phase transition occurs in the temperature range of 189−206 K. The presence of a hysteresis suggests that it is a first-order phase transition, and therefore, there is a possible existence of a RT phase and a LT phase (Figure S3, Supporting Information). The 1-D chain structure of **5** for the RT phase at 240 K is shown in Figure 3, and packing diagrams projected down the *b* and *c* axes are shown in Figure S4 (Supporting Information). The RT phase of **5** crystallizes in the monoclinic space group *C*2/*m*. The structure consists of a neutral 1-D chain with a repeating −Ni−Ni−I− unit lying on the crystallographic 2-fold axis parallel to the *b* axis. The unit cell dimension *b* along the 1-D chain direction consists of three −Ni−Ni−I− units. Crystallographic mirror planes perpendicular to the 1-D chain exist on the I1 atoms and the midpoint of the Ni3 and Ni3′ atoms (i.e., $y = 0, 0.5, 1$). Therefore, the ligand moieties including sulfur atoms of Ni3−Ni3′ units are disordered on two positions, and the twisting directions of two NiS_4 planes of adjacent binuclear Ni1−Ni2 units in the 1-D chain are opposite each other. Two nickel atoms are bridged by four dithiobutanato ligands, and the Ni−Ni distances are Ni1−Ni2 = 2.5336 (8) and Ni3−Ni3′ = 2.5502 (11) Å, which are 0.23 Å shorter than the distances between the mean planes defined by the four sulfur atoms (2.763 (3) and 2.781 (3) Å), respectively. The twist angles between two NiS_4 planes are 28.9 (1)° for a Ni1−Ni2 unit and 27.4 (2)° for a Ni3−Ni3′ unit. Three Ni−I distances are Ni1−I1 = 2.8642(5), Ni2−I2 = 2.9446(6), and Ni3−I2 = 2.9374(6) Å. Taking into account the differences in the Ni−I distances, the valence-ordered state of the nickel atoms in the 3-fold periodic structure may be regarded as $\text{-}I^-\text{-}Ni^{3+}-Ni^{2+}—I^-—Ni^{2.5+}-Ni^{2.5+}-I^-—Ni^{2+}-Ni^{3+}\text{-}I^-\text{-}$. In such a valence state, the unpaired electrons on the adjacent Ni^{3+} sites are expected to take a singlet state due to the strong AF coupling through a bridging iodine atom. However, as will be described in the magnetic property section, the magnetic data of **5** can be fitted as an $S = 1/2$ 1-D AF Heisenberg model. Therefore, compound **5** at RT phase can be assigned to the valence-ordered state close to the AV state. Adjacent $Ni_2(CS_2)_4$ units of Ni1−Ni2 and Ni3−Ni3′ are twisted by ca. 11° from the eclipsed arrangement. The *n*-propyl groups of the dithiobutanato ligands in the Ni1−Ni2 unit have the anti form, whereas those of the Ni3−Ni3′ unit take the gauche form. Therefore, the origin of the 3-fold periodic structure cannot be attributed to the valence ordering of the nickel atoms, but to both the twist of the adjacent dinickel units and the difference in the conformation of the ligands. A similar 3-fold periodic structure was observed for $[Pt_2(RCS_2)_4I]_\infty$ (R = *n*-Pr, *n*-Bu, *n*-Pen).[14−16] From heat capacity measurements, Saito et al. have demonstrated that the first-order phase transition of these platinum complexes originates from the entropy gain by the disorder of the dithiocarboxylate group and alkyl

(32) Bondi, A. *J. Phys. Chem.* **1964**, *68*, 441–451.

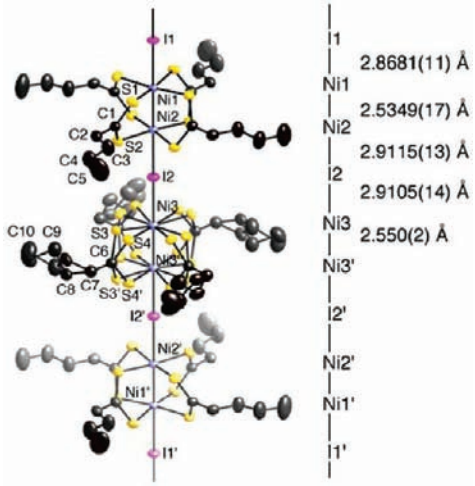

Figure 5. 1-D chain structure of $[Ni_2(n\text{-}BuCS_2)_4I]_\infty$ (**6**) at 290 K with an atomic numbering scheme and relevant interatomic distances (thermal ellipsoids set at the 50% probability level).

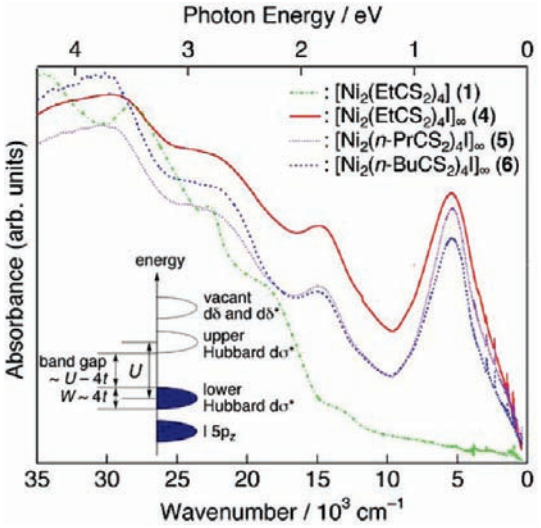

Figure 6. Electronic absorption spectra of $[Ni_2(EtCS_2)_4I]_\infty$ (**4**), $[Ni_2(n\text{-}PrCS_2)_4I]_\infty$ (**5**), and $[Ni_2(n\text{-}BuCS_2)_4I]_\infty$ (**6**) in the solid state (KI pressed disks), together with that of $[Ni_2(EtCS_2)_4]$ (**1**). The inset shows the schematic energy-band structure of $[Ni_2(MeCS_2)_4I]_\infty$ estimated by the unrestricted hybrid DFT calculation (UB3LYP) methods using the dimer and tetramer models.

group of the dithiocarboxylato ligand.[33] The shorter interchain S···S distances in **5** are found to be S(4)···S(4) $(1/2 - x, 1/2 - y, 1 - z) = 4.675(3)$ Å and S(2)···S(2) $(1/2 - x, 1/2 - y, 2 - z) = 4.815(2)$ Å, indicating no interchain S···S contacts.

The space group of **5** changed from $C2/m$ in the RT phase to $C2$ in the LT phase with the first-order phase transition. The 1-D chain structures of **5** in the LT phase at 140 K are shown in Figure 4, and packing diagrams projected down the b and c axes are shown in Figure S5 (Supporting Information). Neutral 1-D chains are parallel to the b axis. The opposite twist of NiS_4 planes between the adjacent dinickel units in the 1-D chain and the difference in conformation of the ligands observed in the RT phase disappeared in the LT phase, and the periodicity of the crystal lattice in the 1-D chain direction changes from a 3-fold −Ni−Ni−I− period in the RT phase to 1-fold in the LT phase. The structure consists of three independent dinickel units; two of them lie on the crystallographic 2-fold axis parallel to the b axis. The Ni−Ni distances are Ni1−Ni2 = 2.5404(11), Ni3−Ni4 = 2.5362(11), and Ni5−Ni6 = 2.5388(8) Å. The Ni−I distances in each dinickel unit are Ni1−I1 = 2.9235(8) and Ni2−I1′ = 2.8994(8) Å, Ni3−I2 = 2.9187(9) and Ni4−I2′ = 2.9084(9) Å, and Ni5−I3 = 2.9108(6) and Ni6−I3′ = 2.9152(7) Å, respectively. Taking into account the distinct difference in Ni−I distances, the valence-ordered state of **5** in the LT phase should be assigned to a CP state of $—Ni^{(2.5-\delta)+}—Ni^{(2.5+\delta)+}\text{-}I^-—Ni^{(2.5-\delta)+}—Ni^{(2.5+\delta)+}\text{-}I^-—$ ($\delta \ll 0.5$) close to the AV state, similarly to **4** at RT.

Crystal Structure of $[Ni_2(n\text{-}BuCS_2)_4I]_\infty$ (6). In **6**, the latent heat corresponding to the first-order phase transition was not observed in the temperature range of 153−333 K. Compound **6** crystallizes in the tetragonal space group $P4/mnc$. The 1-D chain structure of **6** at 290 K is shown in Figure 5, and packing diagrams projected down the c and a axes are shown in Figure S6 (Supporting Information). The structure consists of a neutral 1-D chain with a repeating −Ni−Ni−I− unit lying on the crystallographic 4-fold axis parallel to the c axis. The unit cell dimension c along the 1-D chain direction is a 3-fold −Ni−Ni−I− period, analogously to the RT phase of **5**. The crystallographic mirror planes perpendicular to the 1-D chain exist on the I1 atom and the midpoints of the Ni3 and Ni3′ atoms (i.e., $z = 0, 0.5, 1$). Therefore, the ligand moieties including sulfur atoms of dinickel Ni3−Ni3′ units are disordered at two positions, and the twisting directions of two NiS_4 planes of adjacent dinickel Ni1−Ni2 units in the 1-D chain are opposite each other. Two nickel atoms are bridged by four dithiopentanato ligands, and the Ni−Ni distances are Ni1−Ni2 = 2.5349(17) and Ni3−Ni3′ = 2.550(2) Å, which are 0.22 and 0.23 Å shorter than the distances between the mean planes defined by the four sulfur atoms (2.758(2) and 2.776(3) Å), respectively. The twist angles between the two NiS_4 planes are 29.16(5)° for the dinickel Ni1−Ni2 unit and 27.51 (10)° for the dinickel Ni3−Ni3′ unit. Three Ni−I distances are Ni1−I1 = 2.8681(11), Ni2−I2 = 2.9115(13), and Ni3−I2 = 2.9105(14) Å. Although there are distinct differences between the Ni−I distances, the valence state should be considered to be the valence-ordered state close to the AV state, since the magnetic data of **6** can be fitted using the $S = 1/2$ 1-D AF Heisenberg model, similar to **5**. Adjacent $Ni_2(CS_2)_4$ units of Ni1−Ni2 and Ni3−Ni3′ are twisted by ca. 5.9° from the eclipsed arrangement, and the direction of the n-butyl groups of the Ni1−Ni2 and Ni3−Ni3′ units are opposite each other. Therefore, for the same reason as for **5**, the origin of the 3-fold periodic structure is not attributed to the valence ordering of the nickel atoms but to both the disorder of the dithiocarboxylate group and the n-butyl group of ligand. The shortest interchain S···S distance in **6** is S(2)···S(2) $(1/2 - y,$

(33) (a) Ikeuchi, S.; Saito, K.; Nakazawa, Y.; Sato, A.; Mitsumi, M.; Toriumi, K.; Sorai M. *Phys. Rev. B* **2002**, *66*, 115110 (7 pages). (b) Saito, K.; Ikeuchi, S.; Nakazawa, Y.; Sato, A.; Mitsumi, M.; Yamashita, T.; Toriumi, K.; Sorai, M. *J. Phys. Chem. B* **2005**, *109*, 2956–2961. (c) Ikeuchi, S.; Saito, K.; Nakazawa, Y.; Mitsumi, M.; Toriumi, K.; Sorai, M. *J. Phys. Chem. B* **2004**, *108*, 387–392.

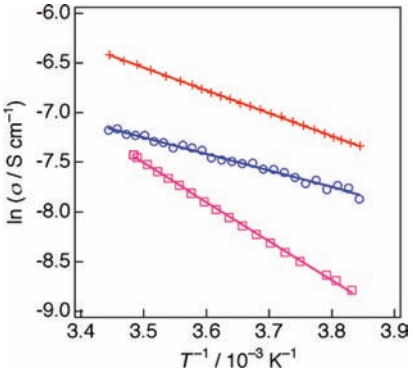

Figure 7. Temperature dependence of the electrical conductivity of **4** (+), **5** (○), and **6** (□).

$1/2 - x, 1/2 - z) = 5.318$ (3) Å, indicating no interchain S···S contacts.

Electronic State. Electronic absorption spectra of **4**−**6** are shown in Figure 6, together with that of **1**. Spectral data are summarized in Table S1 (Supporting Information). The dominant feature of the absorption spectra of **4**−**6** is an intense sharp band centered at 5400 cm^{-1} (670 meV), which is absent from the spectra of **1**−**3** (see Figure S7, Supporting Information). These absorption energies correspond to the optical band gap (E_{opt}), and these values are relatively close to the reported value for $[Ni_2(MeCS_2)_4I]_\infty$ (600 meV).[10b,11a] To elucidate the electronic structure of $[Ni_2(RCS_2)_4I]_\infty$, the UB3LYP method was applied to the model structure of $[Ni_2(MeCS_2)_4I]_\infty$. The highest occupied molecular orbital (HOMO) and lowest unoccupied molecular orbital (LUMO) are composed of a Ni d_{z^2}−Ni d_{z^2} σ^* combination, as depicted in Figure S8 (Supporting Information). The HOMO and LUMO are assigned to a lower Hubbard (LH) dσ^* and an upper Hubbard (UH) dσ^* orbital, that are split by an on-site Coulomb repulsion energy U on a MM unit originating from a strong electron−electron repulsion on the nickel atoms. The schematic energy-band structure of $[Ni_2(RCS_2)_4I]_\infty$ is also shown in Figure 6. The HOMO−LUMO gap corresponding to U is 1.97 eV. The next HOMO is mainly composed of I $5p_z$ orbitals. In order to estimate the transfer energy t and on-site Coulomb repulsion energy U in the bulk, we use the following equations concerning t, U, and an effective exchange integral J: [19a,34]

$$J = \frac{2(E^{LS} - E^{HS})}{\langle \hat{S}^2 \rangle^{HS} - \langle \hat{S}^2 \rangle^{LS}}$$

$$J = -\frac{4t^2}{U}$$

$$\frac{|t|}{U} = \frac{n-1}{2}$$

where E^X and $\langle \hat{S}^2 \rangle^X$ denote a total energy and a total spin angular momentum for the spin state X (X = broken symmetry low-spin (LS) state ($S = 0$) and high-spin (HS) state ($S = 1$)). The equation for J values corrects a spin contamination error in the LS state. And, n is an occupation number of the highest occupied natural orbital, which is a magnetic orbital calculated using the UB3LYP method.[19b] The calculated total energies and total spin angular momenta for LS and HS states are summarized in Table S2 (Supporting Information). From the DFT results and above equations, we obtained $J = -975\ cm^{-1}$, $n = 1.268$, $U = 1.68$ eV, and $t = 0.226$ eV. A result of a similar calculation using the UBH and HLYP method with a tetra-MM unit model also estimated $U = 1.03$ eV and $t = 0.116$ eV.[19a] When we assume that the bandwidth $W = 4t$ is valid since the 1-D Ni MMX system is a 1-D strong electron correlated system, we obtain $4t = 0.904$ eV (0.464 eV for the tetramer model). Accordingly, band energy gap $E_g \sim U - 4t = 0.776$ eV (0.566 eV for the tetramer model). When we assume that the energy difference between the di-MM and tetra-MM models approximates error limits, the E_g is 570−780 meV, which is consistent with the E_{opt} observed for **4** − **6**. Therefore, the intense absorption band observed near 670 meV is attributed to the transition from the LH dσ^* band to the UH dσ^* band.

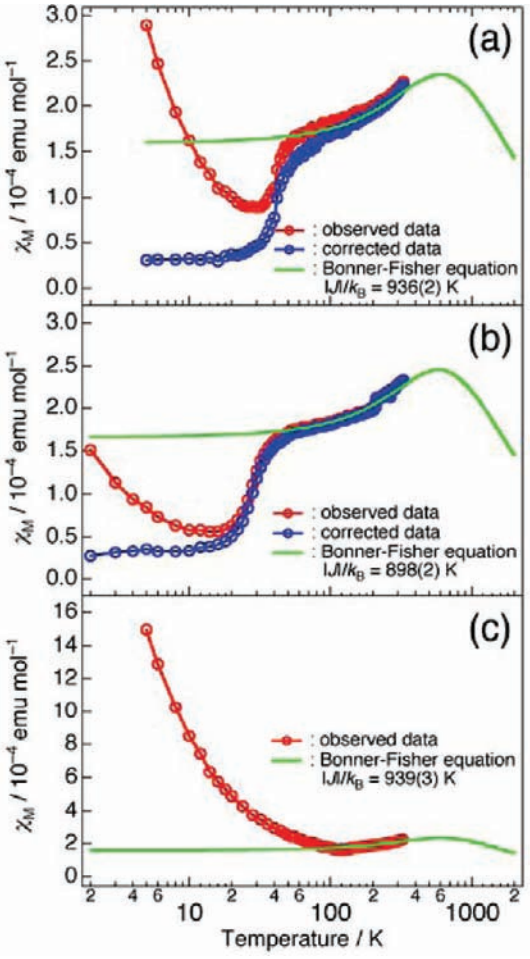

Figure 8. Temperature dependence of the observed (red circles) and corrected (blue circles) magnetic susceptibilities of **4** (a), **5** (b), and **6** (c) and the Bonner−Fisher fits (green lines). The estimated impurity Curie spin contributions are subtracted in the corrected data.

Electrical Conductivity. Temperature dependences of the electrical conductivity σ of **4**−**6** are shown in Figure 7.

(34) (a) Yamaguchi, K.; Kitagawa, Y.; Onishi, T.; Isobe, H.; Kawakami, T.; Nagao, H.; Takamizawa, S. *Coord. Chem. Rev.* **2002**, *226*, 235–249. (b) Yamaguchi, K.; Kawakami, T.; Takano, Y.; Kitagawa, Y.; Yamashita, Y.; Fujita, H. *Int. J. Quantum Chem.* **2002**, *90*, 370–385.

The electrical conductivities of **4**−**6** are 1.6×10^{-3} S cm^{-1} at 290 K, 7.6×10^{-4} S cm^{-1} at 290 K, and 6.0×10^{-4} S cm^{-1} at 287 K, respectively, which are 1 or 2 orders of magnitude smaller than that of $[Ni_2(MeCS_2)_4I]_\infty$ ($\sigma_{RT} = 2.5 \times 10^{-2}$ S cm^{-1}).[11a] Compounds **4**−**6** show typical semiconducting behavior in the temperature range measured, and the activation energies E_a of **4**−**6** estimated from the Arrhenius equation, a plot of ln σ versus T^{-1}, are 198(1), 143(3), and 339(2) meV, respectively. These values are relatively close to that of $[Ni_2(MeCS_2)_4I]_\infty$ (E_a = 100−250 meV).[11a]

Magnetic Properties. The temperature dependences of the magnetic susceptibilities χ_M of polycrystalline samples of **4**−**6** are shown in Figure 8. The common feature of the three compounds is that the susceptibility at room temperature is lower than that expected for one $S = 1/2$ per dimer, and in each case, a lowering is observed as the temperature is lowered. There are slight differences between those of **4** and **5** and that of **6** regarding the appearance of a gradual drop around 50 K for the former two. In addition, **5** exhibits an anomaly in the temperature range 200−212 K, which is associated with the first-order phase transition from the RT phase to the LT phase, as discussed above. Given the one-dimensional structures, we assume an $S = 1/2$ 1-D Heisenberg AF chain model and apply the Bonner−Fisher equation ($H = J \sum S_i \cdot S_{i+1}$)[35] to fit the susceptibility data above 100 K for **4** and 68 K for **5**. The fitting gives exchange coupling constant of $|J|/k_B$ = 936(2) K for **4** and $|J|/k_B$ = 898(2) K for **5**. These J values are in fair agreement with the theoretical J value of −1160 K calculated for $[Ni_2(MeCS_2)_4I]_\infty$ using the UB3LYP method.[19a] The very large J value indicates a very strong AF interaction between the spin of the Ni^{3+} ions through the bridging iodide ion, justifying considerable electronic overlap between the d_{z^2} (Ni) and p_z (I) orbitals. The key feature of the magnetic susceptibility is that it decreases more rapidly below 47 K for **4** and 36 K for **5**. The χ_M values of **4** and **5** take a minimum at about 30 and 16 K, respectively, and then show an increase due to the presence of paramagnetism originating from impurities or lattice and end-of-chain defects. Assuming that the impurities have $S = 1/2$, their concentrations are estimated to be 0.35% for **4** and 0.07% for **5**. By subtracting these contributions from the experimental data, the corrected χ_M values of **4** and **5** are found to decrease to a small constant value. This rapid decrease in χ_M strongly suggests the possibility of a spin-Peierls (SP) transition.[36−40] A spin-Peierls system undergoes a phase transition at T_{sp}, where for $T < T_{sp}$ a temperature-dependent structural dimerization takes place, creating an opening of a spin gap between the singlet and triplet spin states. To date, numerous spin-Peierls materials have been reported, as represented by the organic system TTF−CuBDT[37] and the inorganic system $CuGeO_3$.[38] The exchange constants and transition temperatures are $|J|/k_B$ = 77 K and T_{sp} = 12 K for TTF−CuBDT and $|J|/k_B$ = 120 K and T_{sp} = 14 K for $CuGeO_3$. On the other hand, α′-NaV_2O_5 was also considered a possible inorganic spin-Peierls system with a large exchange coupling constant of $|J|/k_B$ = 560 K and a high transition temperature T_c = 35.3 K,[39a−39c] but more recent studies have revealed that this phase transition may be a novel cooperative phase transition associated with valence ordering, lattice dimerization, and spin-gap formation.[39d,39e] The spin Hamiltonian of the spin-Peierls phase below T_{sp} may be described by the alternating AF chain:

$$H = J' \sum [S_{2i} \cdot S_{2i-1} + \gamma S_{2i} \cdot S_{2i+1}]$$

γ is the alternation parameter, where $\gamma = 1$ corresponds to a uniform chain limit, while $\gamma = 0$ corresponds to the dimer limit. According to the analysis by Ohama et al.,[39c] which is based on the theory of Bulaevskii,[41] the LT magnetic susceptibility is approximated by

$$\chi = \frac{Ng^2\mu_B{}^2\alpha}{k_B T} \exp(-J'\zeta/T)$$

where α and ζ are parameters that depend on the alternating parameter γ and approach unity as $\gamma \rightarrow 0$ (the dimer model) and approach zero as $\gamma \rightarrow 1$ (the uniform chain model). As shown in Figures S9 and S10 (Supporting Information), by fitting the equation to a ln $\chi_M T$ versus T^{-1} plot, the estimated value of $J'\zeta$, which corresponds to an excitation energy gap Δ, is 95(7) K for **4** and 77(2) K for **5**. When the lattice dimerizes, the two unequal and alternating J_1 and J_2 values are expressed as follows[37]

$$J_{1,2}(T) = J\{1 \pm \delta(T)\}$$

According to the mean field theory of Pytte, the relationship between $\delta(T)$ and the excitation energy gap $\Delta(T)$ at temperature T is expressed as[42]

$$\delta(T) = \Delta(T)/pJ$$

where the value of p is 1.637. Using this method, we obtain $\delta(T)$ = 0.062 and J_2/J_1 = 0.88 for **4** and $\delta(T)$ = 0.052 and J_2/J_1 = 0.90 for **5**. The values of $2\Delta(0)/k_B T_{sp}$ of **4** and **5** are 4.04 and 4.28, respectively, which are larger than the value of the typical spin-Peierls materials (TTF-CuBDT, MEM-$(TCNQ)_2$,[43] and $CuGeO_3$) that satisfy

(35) Estes, W. E.; Gavel, D. P.; Hatfield, W. E.; Hodgson, D. J. *Inorg. Chem.* **1978**, *17*, 1415–1421.
(36) Bray, J. W.; Interrante, L. V.; Jacobs, I. S.; Bonner, J. C. In *Extended Linear Chain Compounds*; Miller, J. S., Ed; Plenum Press: New York, 1983; Vol. 3, Chapter 7.
(37) Bray, J. W.; Hart, H. R.Jr.; Interrante, L. V.; Jacobs, I. S.; Kasper, J. S.; Watkins, G. D.; Wee, S. H.; Bonner, J. C. *Phys. Rev. Lett.* **1975**, *35*, 744–747.
(38) (a) Hase, M.; Terasaki, I.; Uchinokura, K. *Phys. Rev. Lett.* **1993**, *70*, 3651–3654. (b) Nishi, M.; Fujita, O.; Akimitsu, J. *Phys. Rev. B* **1994**, *50*, 6508–6510.
(39) (a) Isobe, M.; Ueda, Y. *J. Phys. Soc. Jpn.* **1996**, *65*, 1178–1181. (b) Fujii, Y.; Nakao, H.; Yosihama, T.; Nishi, M.; Nakajima, K.; Kakurai, K.; Isobe, M.; Ueda, Y.; Sawa, H. *J. Phys. Soc. Jpn.* **1997**, *66*, 326–329. (c) Ohama, T.; Isobe, M.; Yasuoka, H.; Ueda, Y. *J. Phys. Soc. Jpn.* **1997**, *66*, 545–547. (d) Fagot-Revurat, Y.; Mehring, M.; Kremer, R. K. *Phys. Rev. Lett.* **2000**, *84*, 4176–4179. (e) Ohwada, K.; Fujii, Y.; Katsuki, Y.; Muraoka, J.; Nakao, H.; Murakami, Y.; Sawa, H.; Ninomiya, E.; Isobe, M.; Ueda, Y. *Phys. Rev. Lett.* **2005**, *94*, 106401 (4 pages).
(40) (a) Obertelli, S. D.; Friend, R. H.; Talham, D. R.; Kurmoo, M.; Day, P. *J. Phys.: Condens. Matter* **1989**, *1*, 5671–5680. (b) Kurmoo, M.; Green, M. A.; Day, P.; Bellitto, C.; Staulo, G.; Pratt, F. L.; Hayes, W. *Synth. Met.* **1993**, *55*−*57*, 2380–2385.
(41) Bulaevskii, L. N. *Sov. Phys. Solid State* **1969**, *11*, 921–924.
(42) Pytte, E. *Phys. Rev. B* **1974**, *10*, 4637–4642.
(43) Huizinga, S.; Kommandeur, J.; Sawatzky, G. A.; Thole, B. T.; Kopinga, K.; de Jonge, W. J. M.; Roos, J. *Phys. Rev. B* **1979**, *19*, 4723–4732.

Table 3. Parameters Defining Some Spin-Peierls Systems

Compound	$\|J\|/k_B$	$\Delta(0)$/K	T_{sp} / K	η'	$2\Delta(0)/k_BT_{sp}$	ref
TTF-CuBDT	77	21	12	0.195	3.50	37
MEM-$(TCNQ)_2$	106	28	17.7	0.209	3.16	36, 43
$CuGeO_3$	120	24.5	14	0.146	3.50	38
α'-NaV_2O_5	560	113.7	35.3	0.079	6.44	39
4	936(2)	95(7)	47	0.063	4.04	this work
5	898(2)	77(2)	36	0.050	4.28	this work

the BCS formula $2\Delta(0)/k_BT_{sp} = 3.53$ but are smaller than that of α'-NaV_2O_5 (6.44).[39b] This discrepancy of $2\Delta(0)/k_BT_{sp}$ is attributed to the larger fluctuation effects compared to ordinary spin-Peierls materials. According to the theory of Cross and Fisher,[44] T_{sp} is given by

$$T_{sp} = 0.8J\eta'$$

where η' is the spin−lattice coupling constant, and $\eta' = 0.063$ for **4** and 0.050 for **5**, which is smaller than the value of typical spin-Peierls materials (0.195, 0.209, and 0.146 for TTF-CuBDT, MEM-$(TCNQ)_2$, and $CuGeO_3$) but is relatively close to the value of α'-NaV_2O_5 (0.079). The phase-transition temperatures of **4** and **5** are suppressed since the coupling between the spin and lattice system is weak due to the large 1-D fluctuations. Parameters defining spin-Peierls systems are listed in Table 3.

On the other hand, the magnetic susceptibility of **6** gradually decreases with a lowering of the temperature, as shown in Figure 8c, and shows a broad minimum at around 135 K. When the experimental data above 140 K are fitted by the Bonner−Fisher equation, $|J|/k_B$ is estimated to be 939(3) K. Below 135 K, χ_M rapidly increases with a lowering of the temperature. Assuming that the increase of χ_M below 50 K is originated from the impurity spin, the impurity spin concentration is estimated to be 1.8%. However, the origin is considered not to be impurity spin but another factor, since this value is much larger than those of **4** and **5**. Saito et al. observed a broad thermal anomaly in the heat capacity measurement of **6**, which is attributed to a higher-order phase transition around 135 K.[45] Therefore, it is reasonable to assume that the structural modulation occurs with the higher-order phase transition, and the magnetic defects giving free spins would be formed in the 1-D chain below 135 K. As a consequence, a spin-Peierls transition appears to be suppressed in **6**.

Synchrotron Radiation X-ray Crystallography. A spin-Peierls system undergoes a lattice instability at T_{sp}, and when $T < T_{sp}$, the system dimerizes and the spin gap opens. To examine the appearance of superlattice reflections originating from lattice modulation due to the dimerization of magnetic centers, synchrotron radiation X-ray diffraction experiments of compounds **4** and **5** were performed using the BL02B1 beamline at SPring-8. Figure 9 and Figure S11 (Supporting Information) show the X-ray diffraction photographs of **4** taken at 50−25 K. Although, in the case of $[Pt_2(RCS_2)_4I]_\infty$ (R = Et, *n*-Pr), X-ray diffuse scattering originating from the valence ordering with a 2-fold repetition length of a −Pt−

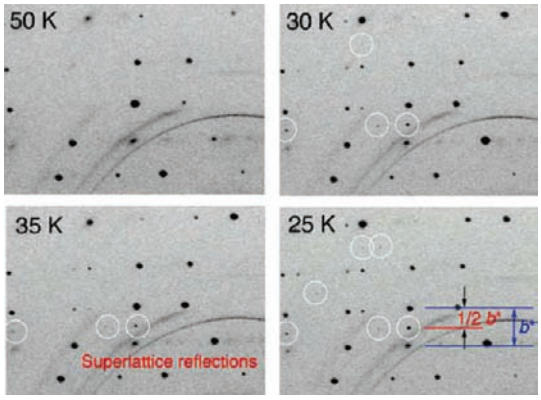

Figure 9. X-ray diffraction photographs of $[Ni_2(EtCS_2)_4I]_\infty$ (**4**) taken at different temperatures. Axis *b** (1-D chain direction) is vertical in these photographs. The diffuse circular lines originate from the carbon fiber mounting a single crystal.

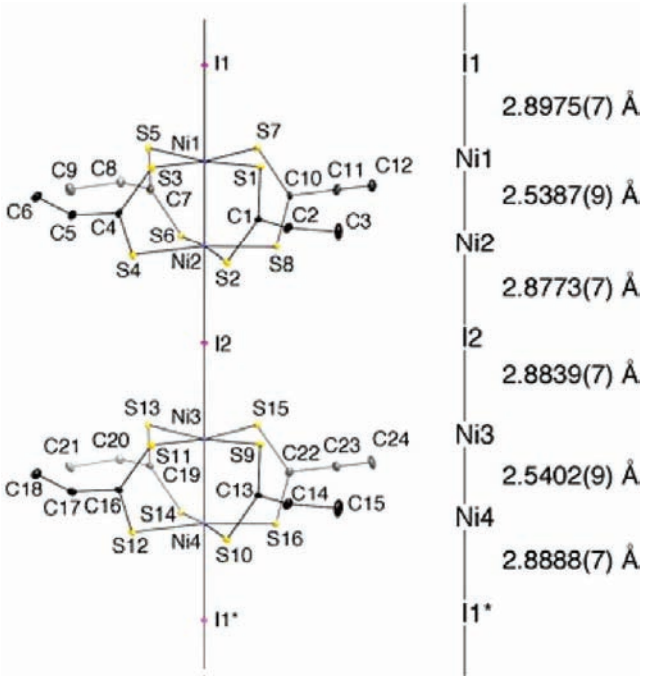

Figure 10. 1-D chain structure of $[Ni_2(EtCS_2)_4I]_\infty$ (**4**) at 26 K with an atomic numbering scheme and relevant interatomic distances (thermal ellipsoid set at the 50% probability level).

Pt−I− unit has been observed,[13−15,17a] the compounds **4** and **5** did not show X-ray diffuse scattering. New reflections clearly appear in the photographs taken below 35 K, indicating a 2-fold superstructure. The number and intensities of the superlattice reflections increase as the temperature is lowered. The unit cell along the *b* axis doubles, which strongly implies that the lattice dimerizes along the −Ni−Ni−I− chain. In order to determine the LT superstructure of **4**, synchrotron radiation crystal structure analysis was performed for data taken at 26 K. When the superlattice reflections are included, the supercell can be indexed by $a_{super} = -0.5a - 0.5b$, $b_{super} = 0.5a - 1.5b$, and $c_{super} = 0.5a + 0.5b + c$, and the space group changes from $C2/c$ to $P\bar{1}$. Figure 10 shows the 1-D chain structure of the superstructure of **4** at 26 K. Packing diagrams projected down the *c* and *a* axes are shown in Figure S12 (Supporting Information).

(44) Cross, M. C.; Fisher, D. S. *Phys. Rev. B* **1979**, *19*, 402–419.
(45) Ikeuchi, S.; Yamamura, Y.; Yoshida, Y.; Mitsumi, M.; Toriumi, K.; Saito, K. Unpublished.

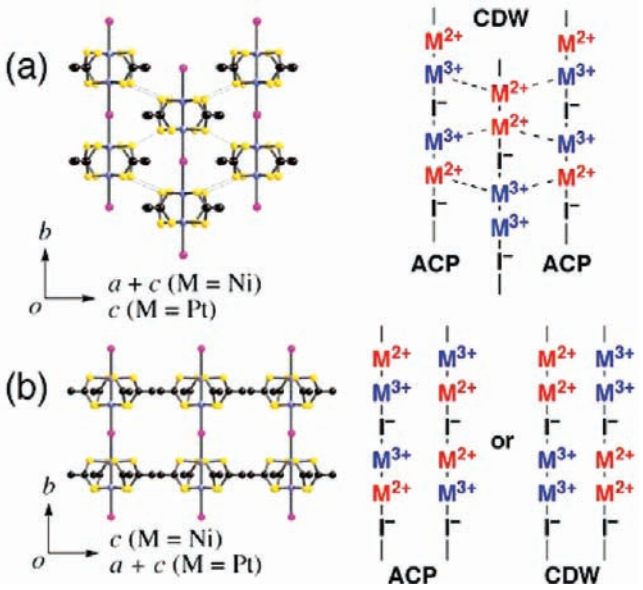

Figure 11. Relationship between relative arrangement of 1-D chains in the crystal of $[M_2(MeCS_2)_4I]_\infty$ (M = Ni, Pt) and possible two-fold periodic valence ordering to minimize the Coulomb repulsion.

Two crystallographically independent $[Ni_2(EtCS_2)_4I]$ units exist in a unit cell of **4** in the LT phase, and the periodicity of the crystal lattice is a 2-fold −Ni−Ni−I− period. The two Ni−Ni distances are almost the same (Ni1−Ni2 = 2.5387(9) and Ni3−Ni4 = 2.5402(9) Å), but there are two different Ni−I bond distances. The short Ni−I distances (Ni2−I2 = 2.8773(7) and Ni3−I2 = 2.8839(7) Å) are about 0.013 Å less than those of the long Ni1−I1 = 2.8975(7) and Ni4−I1* = 2.8888(7) Å). The 2-fold superstructure originates from the different Ni−I distances since the structures of the two crystallographically independent $[Ni_2(EtCS_2)_4I]$ units are approximately equal and twisting does not occur between binuclear units. The doubling of the lattice periodicity and the increase of the superlattice reflections on lowering the temperature strongly support the spin-Peierls transition at 47 K. The Ni−Ni and Ni−I distances indicate that the valence-ordered state in the LT phase is the ACP state of $—Ni^{(2.5-\delta)+}—Ni^{(2.5+\delta)+}$-$I^-$-$Ni^{(2.5+\delta)+}—Ni^{(2.5-\delta)+}—I^-—$ ($\delta \ll 0.5$). This phase transition is a spin-Peierls transition that accompanies the rearrangement of the valence ordering. In diplatinum compounds $[Pt_2(RCS_2)_4I]_\infty$ (R = Et, *n*-Bu), the difference between the long and short Pt−I distances, that characterizes the degree of the lattice distortion, is 0.029 and 0.066 Å, respectively.[14] The lattice distortion of **4** is therefore smaller than those of the diplatinum compounds. The diplatinum compounds can be largely polarized due to the larger span of the $5d_{z^2}$ orbitals, whereas the degree of charge-polarization of the nickel compound is small since this material tends to retain a valence state close to the AV state due to the strong electron−electron correlation effect on the $3d_{z^2}$ orbitals of the nickel atoms. Compound **5** also exhibits superlattice reflections at the positions of $1/2b^*$ corresponding to the 2-fold −Ni−Ni−I− period at temperatures below T_{sp} = 36 K. However, attempts to index the superlattice reflections were unsuccessful because of their very weak intensities (Figure S13, Supporting Information). Therefore, we were only able to resolve an averaged crystal structure of **5** below 36 K. The 1-D chain structures of **5** at 31 K are shown in Figure S14 (Supporting Information). Packing diagrams projected down the *b* and *c* axes are shown in Figure S15 (Supporting Information). The averaged structure is in the monoclinic space group *C*2, which is the same space group as the structure in the LT phase at 140 K.

We have demonstrated by the crystal structure analyses of the superstructure that the valence-ordered state of $[M_2(EtCS_2)_4I]_\infty$ (M = Ni, Pt) is ACP.[14] In contrast, the spin-Peierls transition has not been observed in $[Ni_2(MeCS_2)_4I]_\infty$, and the superlattice reflections due to the development of the superstructure associated with the 2-fold periodic valence ordering have not been observed in $[M_2(MeCS_2)_4I]_\infty$ (M = Ni, Pt). Finally, we discuss the reason for these results based on the relative arrangement of 1-D chains in the crystal. As shown in Figure 11, there are two types for the arrangements of 1-D chains.[10] Adjacent 1-D chains in arrangement type (a) shift about a half period from each other, whereas the 1-D chains in arrangement type (b) are aligned with the same phase. We argue that the 2-fold periodic valence ordering minimizes the Coulomb repulsion between the 1-D chains. The type (b) arrangement is capable of taking both valence-ordered ACP and CDW states. $[M_2(MeCS_2)_4I]_\infty$ (M = Ni, Pt) have relatively short interchain S···S contacts in the type (a) arrangement, and these compounds are considered to have two-dimensional interactions.[10] When a 1-D chain takes the ACP state in type (a), adjacent 1-D chains should take the CDW state to minimize the Coulomb repulsion. As a result, it is presumed that these compounds would have difficulty adopting the superstructure associated with the 2-fold periodic valence ordering, and consequently, $[Ni_2(MeCS_2)_4I]_\infty$ does not show the spin-Peierls transition associated with the ACP state. On the other hand, $[Ni_2(RCS_2)_4I]_\infty$ (R = Et, *n*-Pr) have the ability to adopt 2-fold periodic valence ordering since the one-dimensionality of these compounds becomes more pronounced with the elongation of the alkyl chain of the dithiocarboxylato ligands.

4. Conclusions

The partial oxidation of $[Ni^{II/II}_2(RCS_2)_4]$ (R = Et (**1**), *n*-Pr (**2**), and *n*-Bu (**3**)) with molecular iodine affords the MMX chain compounds $[Ni^{II/III}_2(RCS_2)_4I]_\infty$ (R = Et (**4**), *n*-Pr (**5**), and *n*-Bu (**6**)), respectively. They possess neutral 1-D chain structures with a repeating −Ni−Ni−I− unit and are characterized as Mott−Hubbard semiconductors. They display markedly different magnetic behaviors at low temperatures, where the magnetic susceptibility of **4**−**6** can be fitted to an $S = 1/2$ 1-D Heisenberg AF chain with $|J|/k_B$ = 898(2)−939 (3) K. Compounds **4** and **5** undergo the spin-Peierls transition at relatively high transition temperatures of T_{sp} = 47 and 36 K, respectively. However, the spin−lattice coupling constants of **4** and **5** are small compared to those of a typical spin-Peierls systems and are due to the large 1-D fluctuation characteristics of MMX chain compounds. In contrast, **6** exhibits a rapid increase in the magnetic susceptibility below 50 K, which would be ascribed to free spins originating from the magnetic defects formed by the structural modulation with

the higher-order phase transition around 135 K. Compounds **4** and **5** show superlattice reflections corresponding to the development of new periodic ordering with 2-fold repeating lengths of the MMX units below T_{sp}. By determining the superstructure of **4** in the spin-Peierls state, we have shown that the valence-ordered state changes from the CP state in the RT phase to the ACP state in the LT phase, and this phase transition is a spin-Peierls transition accompanying the rearrangement of the valence ordering. This valence-ordered state of **4** is the same as that of $[Pt_2(RCS_2)_4I]_\infty$ (R = Et, *n*-Bu).[14] However, the origin of the transition is apparently different, although the Ni and Pt $[M_2(RCS_2)_4I]_\infty$ analogues are structurally similar. The transition to the ACP state in $[Pt_2(n\text{-}BuCS_2)_4I]_\infty$ is accompanied by a rapid decrease in the conductivity and magnetic susceptibility and is then assigned to a regular electronic Peierls transition. From these experimental results, we have concluded that the electron−lattice interaction is dominant in $[Pt_2(RCS_2)_4I]_\infty$, whereas the solid-state properties of $[Ni_2(RCS_2)_4I]_\infty$ are governed by the strong electron correlation of the Ni atoms. The results confirm the dependence of the solid-state properties on the central metal ions.

Acknowledgment. This work was supported in part by a Grant-in-Aid for Young Scientists (No. 10740307) from the Ministry of Education, Culture, Sports, Science and Technology, Japan, the Mitsubishi Chemical Corporation Fund, Grant for Basic Science Research Projects of the Sumitomo Foundation, and the CNRS-France. Use of SPring-8 was supported by Japan Synchrotron Radiation Institute under Power User Priority Program (2003B2888-PU1-np). XPS measurements were supported by a "Nanotechnology Support Project" of the Ministry of Education, Culture, Sports, Science, and Technology (MEXT) of Japan.

Supporting Information Available: X-ray crystallographic information files in CIF format for compounds **4**−**6** and additional characterization data. This material is available free of charge via the Internet at http://pubs.acs.org.